The Derivation of Consistent Fields of Wind and Geopotential Height from Mesoscale Rawinsonde Data

J. C. FANKHAUSER

National Center for Atmospheric Research,[1] *Boulder, Colo. 80303*

(Manuscript received 9 November 1973, in revised form 13 June 1974)

ABSTRACT

With an attainable height resolution of no better than ±10 m from individual soundings, direct analysis of geopotential height gradient from mesoscale rawinsonde ascents could not be expected to produce reliable results. A method is presented for deriving a height field which incorporates the carefully analyzed horizontal winds measured by an upper air network specifically designed to study severe thunderstorms. Three-dimensional distributions of wind, temperature and moisture content are obtained as a function of time using a combination of subjective and objective analysis techniques, which take account of departure from scheduled release time, differing ascent rates, and the horizontal drift of balloons during ascent.

The vertical component of air motion is computed from the kinematic approach. Adjustments are applied to divergence estimates to achieve physically realistic results for vertical motion in the upper troposphere. Errors in the horizontal wind components are likewise altered for consistency by assuming that they affect only the divergent part of the flow. The three-dimensionally consistent array of velocity components is used to evaluate the complete horizontal divergence equation to obtain the geopotential Laplacian as a residual, which, when integrated numerically, yields the horizontal height perturbations associated with the mesoscale winds. Results obtained from application of these techniques to rawinsonde data collected in a squall line case appear to be in qualitative agreement with recognized thunderstorm airflow and pressure distributions. Comparative magnitudes of individual terms in the divergence equation demonstrate that the balance approximation is inadequate for diagnosing the dynamics of mesoscale convective motions.

1. Introduction

The National Severe Storms Laboratory (NSSL) has been collecting mesoscale rawinsonde observations in the presence of convective storms in Oklahoma since 1966. These data afford a unique opportunity to examine the dynamical interactions between synoptic- and convective-scale motions. To do so adequately, however, requires knowledge of the pressure gradient forces, or when pressure is chosen as the vertical coordinate, the gradient of geopotential height.

Evaluation of geopotential height from individual soundings is inherently limited by the accuracy of the surface pressure measurement, which for the earliest NSSL data is no better than ±1 mb (Barnes *et al.*, 1971). The associated height discrepancies amount to ±10 m. In assessing the sensing capabilities of the GMD-1 sounding system (the type used in the NSSL network), Lenhard (1973) found rms height errors which increased from about 2 m at low levels to as much as 12–15 m near the tropopause. Madden *et al.* (1971) present data comparing GMD-1 height computations with coincident balloon tracking by radar which show that random height errors of 20–30 m are common.

At the mesoscale the combined uncertainties deriving from random error sources and surface pressure bias are therefore likely to be larger than the horizontal height gradients that must be resolved, and a direct analysis of the geopotential height field could not be expected to produce reliable results. An earlier analysis (Fankhauser, 1969) has established the consistency between thermodynamic and kinematic features resolved by the NSSL sounding network. This paper presents a method for deriving a height field that incorporates the carefully analyzed horizontal wind field.

2. Data collection, reduction and analysis

The configuration of the NSSL upper air and surface mesonetworks as they existed in 1966 is shown in Fig. 1. Average spacing between rawinsonde stations was around 85 km and the distance between surface sites was 20–30 km. During a typical research operation, balloons were released at all ten sites simultaneously and tracking was purposely terminated at 100 mb to maintain the desired sounding frequency of 90 min. Raw temperature, moisture and wind data from individual soundings were evaluated at approximately 30-sec intervals (~150 m in the vertical), using a slightly modified version of a computerized

[1] The National Center for Atmospheric Research is sponsored by the National Science Foundation.

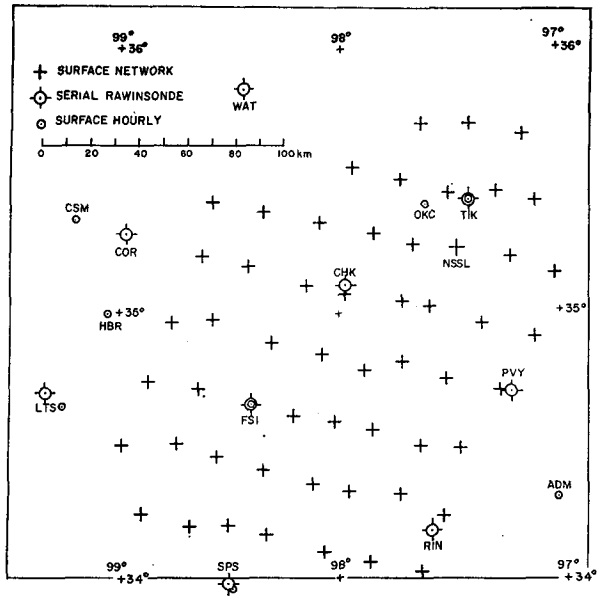

FIG. 1. NSSL surface and upper air networks in 1966. A tenth rawinsonde site was located ~90 km WSW of Altus, Okla. (LTS).

reduction technique developed by Kreitzberg and Brockman (1966).

As the first step in the analysis, data from each station's sounding series were plotted by a computer graphical routine in vertical time sections (with pressure p as vertical coordinate), accounting for the lapse of time during balloon ascent. A typical series for the layer from the surface to 500 mb is shown in Fig. 2, where asterisks are data points and numbers plotted to the left and right are wind speed and direction, respectively. Similar time sections are generated for the layer from 500 to 100 mb, and for the variables potential temperature θ and mixing ratio r.

Time sections such as that in Fig. 2 are subjectively analyzed to obtain the vertical distribution of isotachs, isogons, isentropes and moisture content, as a function of time for each station's series. These fields are converted from analogue to digital form through use of the NCAR Datagrid (Jenne *et al.*, 1972) and the two-dimensional digital data are interpolated after spline curve fitting (Cline, 1973) to extract vertical profiles of all parameters at equal time intervals of 30 min. In addition to the meteorological variables, balloon position with respect to its release point is interpolated in the p-t domain. This is required to compensate for departure from scheduled release time, for differing balloon ascent rates, and for the horizontal drift of the balloons during ascent.

From the interpolated 30-min vertical profiles, 50-mb means of all variables are obtained for 18 layers between the surface and 100 mb. These data are computer-plotted on horizontal sections at the appropriate interpolated balloon position. The horizontal fields for all 18 layers and each synoptic time are then subjectively analyzed for the same parameters as those treated in the time sections. These hand-drawn charts are again converted to digital form and objectively interpolated by the two-dimensional spline operation to obtain horizontal arrays of all data at 10-km intervals on a 240 km×240 km grid. At this stage a complete three-dimensional meteorological data set with time continuity is available for diagnostic treatment.

Examples of the details and scales of features resolvable from the foregoing analysis scheme are given in Fankhauser (1969).

3. Divergence and vertical velocity

From the horizontal wind, $\mathbf{V}=(u,v)_p$, a vertical profile of divergence is calculated at each grid point according to

$$D_k=(\partial u/\partial x+\partial v/\partial y), \tag{1}$$

where the horizontal velocity components are means for a layer k of thickness $\Delta p=50$ mb.[2] Upon invoking the equation of continuity, integration of the divergence profile with respect to pressure yields the vertical component of velocity, ω_p, at the top of each layer:

$$\omega_p=\omega_{p+\Delta p}+D_k\Delta p. \tag{2}$$

As is often the case, the vertical velocity computed from the kinematic technique was found to produce reasonable values at low levels, but led to physically unrealistic results in the upper troposphere. This is attributable primarily to the fact that the quality of wind measurements from a GMD-1 system deteriorates with decreasing elevation angles, due to the combined consequence of strong uniform winds aloft and sounding duration.

O'Brien (1970) developed a scheme for altering the original divergence estimates so that the adjusted profiles satisfy some independently defined boundary conditions on ω at the top and bottom of an atmospheric column. The algorithm chosen is based on the simple hypothesis that divergence errors increase vertically as a linear function of pressure. The equations for the adjusted divergence and vertical velocity are written as

$$D_k'=D_k+\frac{k}{M}(\omega_K-\omega_T)/\Delta p, \tag{3}$$

$$\omega_p'=\omega_p-(\omega_K-\omega_T)\frac{k}{2M}(k+1), \tag{4}$$

where

$$M=\sum_{k=1}^{K}k=\tfrac{1}{2}K(K-1). \tag{5}$$

Here K is the total number of layers and k again

[2] The method for computing divergence in the layer of variable pressure depth immediately overlying the surface is elaborated in Fankhauser (1969).

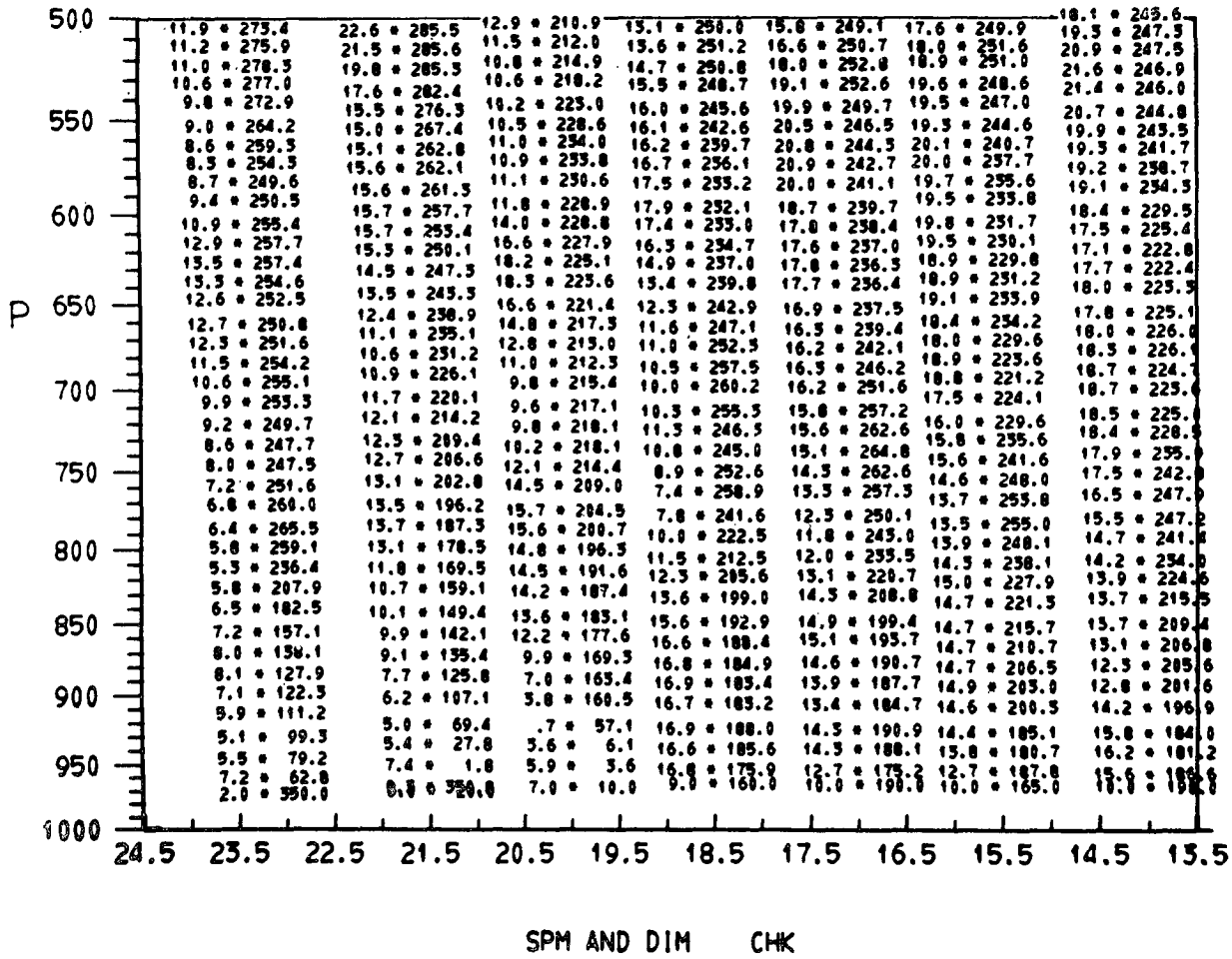

FIG. 2. Computer-generated cross section of raw wind data from serial soundings obtained at Chickasha, Okla. (CHK, in Fig. 1), on 8 June 1966, plotted as a function of time (CST) and pressure p. Asterisks represent data points with wind direction on the right and wind speed (m sec^{-1}) on the left.

denotes individual layers. Boundary conditions on ω_p' are the original estimate of ω_p at the top of the lowest layer and ω_T at 100 mb. In results to be presented later the choice of $\omega_T=0$ is justified by small values obtained from the independent application of the adiabatic vertical velocity equation in the stable lower stratosphere.

We note that application of (3) and (4) achieves the desired end in that essentially no alteration of original computations occurs near the ground, while most of the error is compensated at the highest levels where original estimates are subject to greatest doubt. Divergence and vertical motion adjusted according to (3) and (4) have been subjected to quantitative assessment in atmospheric regimes of varying scale (Fankhauser, 1969; Smith, 1971), and demonstrated results were found to be physically realistic.

4. Adjustment of horizontal wind components

Errors in the horizontal wind components which contributed to the divergence discrepancy, $D''=D'-D$, have yet to be considered. We express the components as originally analyzed in terms of their rotational (nondivergent) and divergent (irrotational) parts,

$$u=u_r+u_d, \quad v=v_r+v_d, \tag{6}$$

and note that operations (3) and (4) leave the rotational part unaltered. We will consider adjustments to only the divergent part, and introduce a function χ, analogous to velocity potential, which satisfies the relation, $D'=\nabla^2\chi'$. Wind discrepancies may then be represented by a function χ'', and the velocity components consistent with the adjusted divergence D' are given by

$$u'=u+\frac{\partial\chi''}{\partial x}, \quad v'=v+\frac{\partial\chi''}{\partial y}, \tag{7}$$

where

$$\nabla^2\chi''=D'-D=D''. \tag{8}$$

To obtain the desired velocity adjustments, (8) is solved numerically by the method of relaxation and the χ'' field is differentiated with respect to x and y.

For the integration we set $\chi''=0$ at the boundaries. This is equivalent to leaving the u component unaltered along boundaries parallel to the x axis and imposing no correction for v along those parallel to the y axis.

We know from (3) that D'', and, hence, adjustments to horizontal components, will be greatest in the uppermost layer. In evaluating the right-hand terms in (7) it is necessary to obtain a solution for (8) in the top layer only, since results for other layers are determined by the weighting factor k/M.

5. Evaluation of the geopotential field[3]

With a three-dimensionally consistent array of velocity components available as a function of time, we are prepared to consider solutions for the associated geopotential field. Neglecting viscous terms, the equations of horizontal motion with pressure as vertical coordinate are

$$\frac{\partial u}{\partial t}+u\frac{\partial u}{\partial x}+v\frac{\partial u}{\partial y}+\omega\frac{\partial u}{\partial p}-fv=-\frac{\partial \phi}{\partial x}, \tag{9}$$

$$\frac{\partial v}{\partial t}+u\frac{\partial v}{\partial x}+v\frac{\partial v}{\partial y}+\omega\frac{\partial v}{\partial p}+fu=-\frac{\partial \phi}{\partial y}. \tag{10}$$

The horizontal divergence equation can be derived by differentiating (9) with respect to x and (10) with respect to y, and adding the two. Combining terms and rearranging gives

$$\text{Balance equation}\begin{cases}\left\{-\nabla^2\phi=-f\left(\frac{\partial v}{\partial x}-\frac{\partial u}{\partial y}\right)\right\}\ \text{Quasi-geostrophic approximation}\\ -2\left(\frac{\partial v}{\partial x}\frac{\partial u}{\partial y}-\frac{\partial u}{\partial x}\frac{\partial v}{\partial y}\right)+\beta u\end{cases}$$
$$+\left(\frac{\partial \omega}{\partial x}\frac{\partial u}{\partial p}+\frac{\partial \omega}{\partial y}\frac{\partial v}{\partial p}\right)+D^2+\left(\frac{\partial D}{\partial t}+u\frac{\partial D}{\partial x}+v\frac{\partial D}{\partial y}+\omega\frac{\partial D}{\partial p}\right). \tag{11}$$

Terms usually neglected in dealing with large-scale motions are the twisting term, and those involving D^2 and the individual derivative of D.

With u, v, ω and D defined, it is possible to evaluate the geopotential Laplacian $\nabla^2\phi$ as a residual of all right-hand terms in (11). To obtain ϕ we integrate $\nabla^2\phi=-F(x,y)$ numerically. The value of ϕ at the boundaries is imposed by assuming that normal wind components there obey the geostrophic approximation, i.e.,

$$\frac{\partial \phi}{\partial x}=fv \quad \text{and} \quad \frac{\partial \phi}{\partial y}=-fu,$$

along boundaries parallel to the x and y axes, respectively.

6. A test of the analytical technique

a. The convective situation

The foregoing analytical procedures were tested in the squall line case of 8 June 1966. Fig. 3 shows the synoptic-scale surface streamlines and radar echoes in the early stages of squall line development. Numerous tornadoes and funnel clouds were observed in Kansas and Oklahoma between 1100 and 2100 CST and the large echo complex shown in north central Kansas produced the highly destructive Topeka, Kan., tornado at about 1930 CST (Galway, 1966). Endlich and Mancuso (1968) subjected the synoptic weather data for this day to objective analysis, and attendant large-scale upper air features are elaborated there. We will restrict our attention to the mesoscale air flow as resolved within the area delineated by the dashed box in south central Oklahoma. The observational period covered by serial rawinsonde releases extended from 1100 through 2300 CST. A total of 76 soundings was obtained from the 10 network sites involved. A typical series is presented in Fig. 2.

Fig. 4 shows examples of the mesoscale streamlines analyzed at low and high levels as the squall line evolved through formative, mature and decaying stages. The winds and flow patterns represent 50-mb means at the two selected levels and are derived according to procedures outlined in Section 2. Map times correspond closely to the actual scheduled balloon release at the nine stations shown (a tenth lies off the grid to the southwest). Radar echo intensity contours at 10-db intervals above minimum detectable signal show the location and development of convective activity during the 3-hr period.

At low levels, strong boundary layer convergence along the confluent asymptote had been acting for some 3–4 hr prior to the appearance of the first radar echoes at about 1600. Large individual thunderstorm cells observed at 1700 had formed into a nearly continuous band by 1830, and at 2000 the intense squall

[3] The prime notation, denoting adjusted variables, will be dropped in the ensuing discussion.

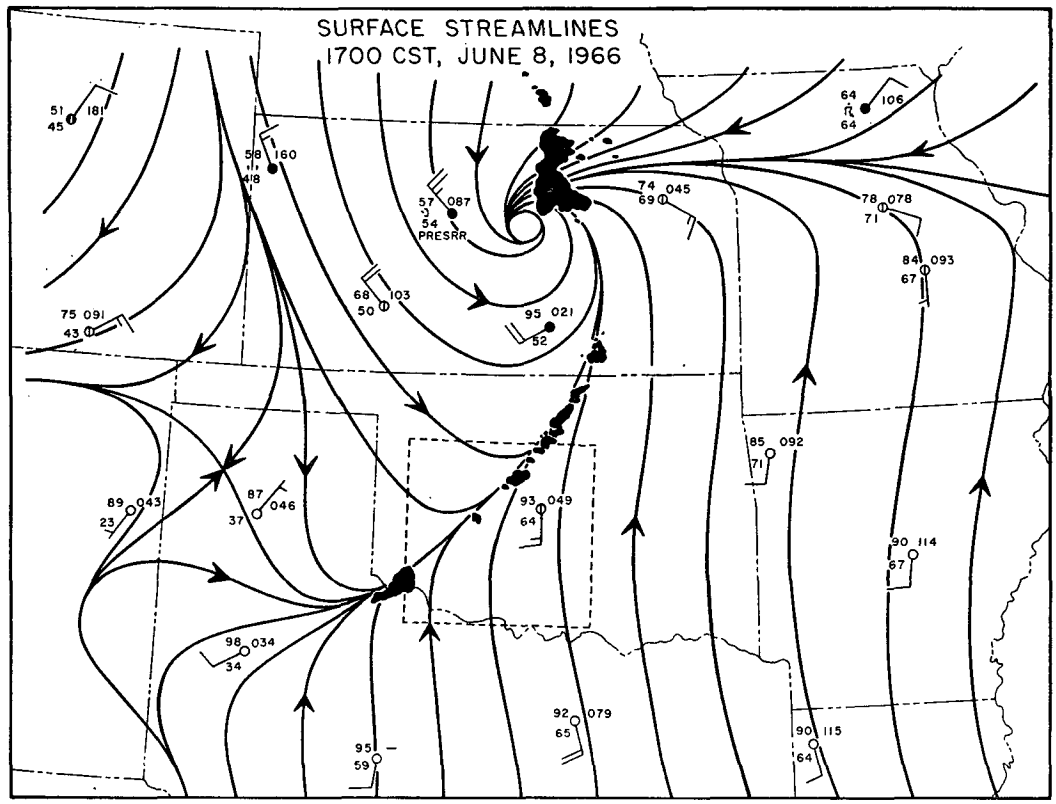

FIG. 3. Surface streamlines at 1700 CST 8 June 1966. Thunderstorm precipitation echoes are composited from National Weather Service WSR-57 radars located at Wichita, Kan., and Amarillo, Tex. Dashed box shows boundaries of NSSL network as shown in Fig. 1. Winds are in knots.

line had become disorganized and showed signs of the dissipation which eventually occurred by 2300.

Streamline analyses in the 250–200 mb layer show that with respect to direction the flow was essentially unperturbed at and prior to 1700, although some speed divergence did exist over the northeast part of the grid. By 1830 a distinct diffluent zone appeared ahead of the large isolated thunderstorm off the southwest corner of the grid, but the flow is still relatively undisturbed in the immediate vicinity of the main squall line. The eventual effect of the line convection on the flow aloft, however, is dramatically revealed by the strong diffluence shown at 2000 CST. This sequence of events aloft suggests that upper tropospheric divergence, long considered a prognostic indicator of severe thunderstorms (Beebe and Bates, 1955; House, 1958) may at times be a result and not necessarily the precursor of organized convective activity.

In the subjective streamline and isotach analyses, careful attention was given to preserving the continuity of features in time and space. Details drawn at lower levels are strongly influenced by surface conditions where observations are four times more dense than aloft. As the analysis was carried from low to higher levels, features such as the location of the surface confluence zone were used in positioning the high-level regions of streamline diffluence. This, of course, is motivated by the need to locally satisfy mass continuity in a vertical air column. Although wind discontinuities may be subjectively misplaced by as much as one grid interval, the impact on results to be presented later would be reflected only as a phase shift. Magnitudes of perturbations are not greatly influenced, since forcing is occurring on scales larger than one or two grid intervals.

In the 250–200 mb layer, separation of winds plotted at the interpolated balloon positions from their release points emphasizes the need to consider horizontal balloon translation during ascent. Maximum displacement amounts to 50 km or as much as five times the computational grid interval.

b. Resolved divergence and vertical velocity

Fig. 5 is a cross section taken normal to the squall line at 1830 showing the vertical distribution of divergence and vertical velocity computed according to procedures outlined in Section 3. Over the squall line axis strong convergence in the subcloud layers is nearly compensated by divergence in the upper tropospheric layers. This distribution leads to a core of

maximum vertical velocity extending from 800 mb to just over 400 mb. On the up and downwind sides the positive and negative divergence couplets are reversed in the vertical, leading to weaker subsident motions in the near-cloud mid-tropospheric regime.

It is of some interest here to compare the scale of resolved kinematic features to those of the squall line. The average width of the radar band at 1830 in Fig. 4 is 20–25 km, while the region of ascending motion as shown in Fig. 5 has lateral dimensions on the order of 40–50 km. Thus, the calculated scale lengths are about half the spacing between rawinsonde sites and twice the surface network interval. A purely objective treatment of the upper air data would restrict definition to wavelengths that are twice the station interval (~175 km). Apparently, the combined application of subjective and objective analysis produces results that pertain to a scale lying somewhere between convective- and synoptic-scale circulations.

c. Evaluation of the divergence equation

At the time corresponding to the cross section in Fig. 5, wind data synthesized according to procedures described in Sections 2–5 were applied in evaluating the right-hand terms in (11). Results were obtained for all grid points in the 16 horizontal layers between 950 and 150 mb. The local derivative of D was computed from values at 1800 and 1900 CST.

Table 1 lists the vertical distribution of the individual terms[4] of (11) at a grid point located slightly ahead (southeast) of the squall line axis (see Figs. 5 and 6). As might be anticipated from the configurations in Fig. 5, the terms involving D^2 and the individual derivative of D dominate in the lowest and highest layers, while the twisting term dominates in middle layers where the horizontal gradient of ω is

[4] The βu term, being one to two orders of magnitude smaller than others in (11), is not included in Table 1.

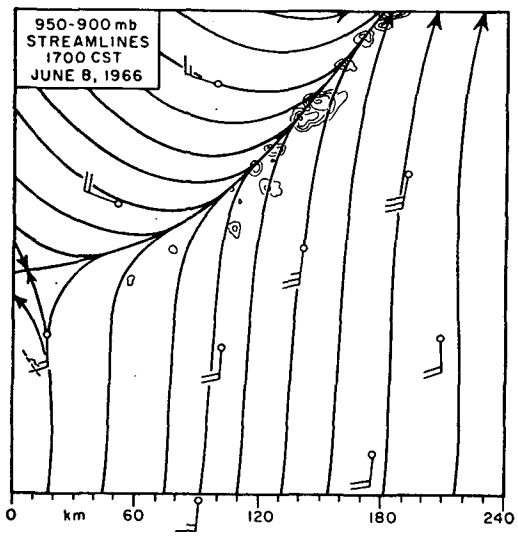

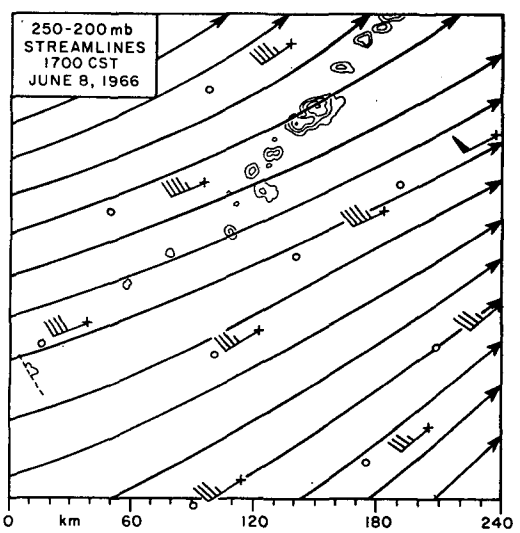

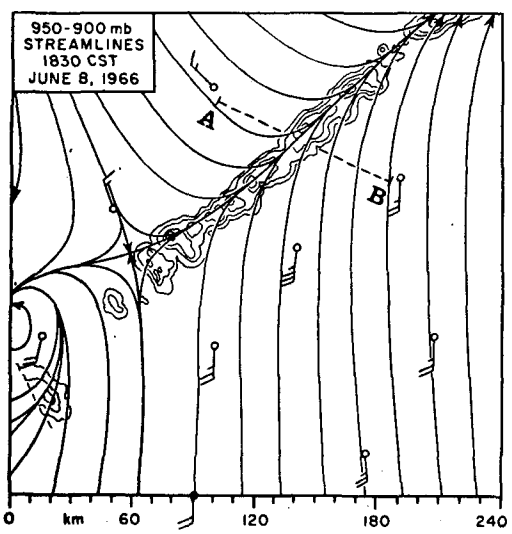

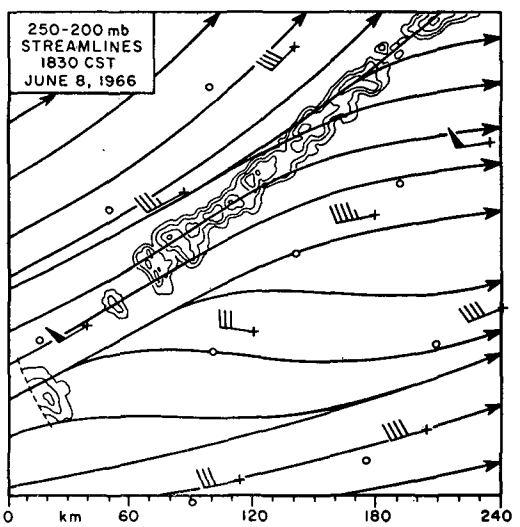

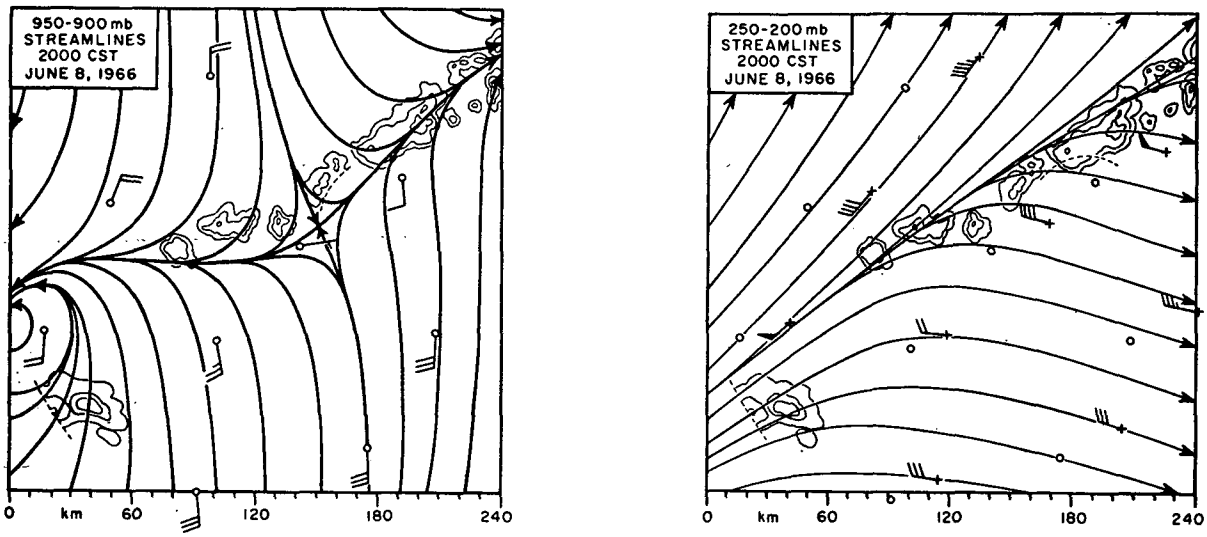

FIG. 4. Streamlines of 50-mb layer-averaged airflow at low (950–900 mb) and high (250–200 mb) levels for 1700, 1830 and 2000 CST 8 June 1966. Circles represent station location and crosses interpolated balloon position. Since map times correspond closely to actual balloon release times, winds at low levels are plotted essentially on the release point, while aloft considerable separation exists between balloon position and station location. One full wind barb represents 5 m sec^{-1}. Radar echoes, as recorded by the NSSL WSR-57 10-cm research radar, are shown at 10-dB intensity levels. Line AB on the map for 1830 CST at 950–900 mb shows the location and orientation of the cross section in Fig. 5.

large. At all levels in the vicinity of the squall line the Jacobian and vorticity terms are small compared to those involving divergence and vertical velocity. Individual terms at grid points well removed from the active convection were found to be small and of comparable magnitude, with no particular dominance indicated from layer to layer.

The largest difference between $|\mathbf{V}|$ and $|\mathbf{V}'|$ resulting from the horizontal velocity adjustments discussed in Section 4 was 2.6 m sec^{-1}. This probably represents a reasonable measure of the 2σ level in a normal distribution about zero, so that discrepancies on the order of ± 1 m sec^{-1} might be taken as the standard deviation. If the magnitude of errors in the rotational component $[(u_r,v_r)$ in (6)] are comparable to those of the divergent part, we may consider possible effects on terms in Table 1. The Jacobian and vorticity terms are the only ones involving rotational derivatives and introduction of a random velocity error of 1 m sec^{-1} in these terms produced less than order-of-magnitude changes. Thus, failure to consider possible errors in the rotational components has no significant effect on the results in Table 1.

The balance equation is invoked when it is desirable to suppress high-frequency waves usually associated with large values of divergence. The magnitude of the terms involving divergence indicates that in this case the balance approximation would be inadequate for dealing with intense convective circulations.[5] Retention of the divergence terms, however, raises the question of the validity of the hydrostatic assumption, implicitly embodied in the development of the divergence equation as the vertical equation of motion. Vertical accelerations, associated with the magnitude of vertical velocities shown in Fig. 5, can be shown to be two to three orders of magnitude less than the acceleration of gravity; hence, incorporation of the hydrostatic assumption does not significantly affect these results.

[5] For a comprehensive discussion of how individual terms in the divergence equation relate to severe thunderstorm development, the reader is referred to House (1961).

d. The resolved relative height fields

Using the residual formed from the sum of right-hand terms in (11) as the forcing function, the relative height perturbations are obtained by numerical integration as outlined in Section 5. Fig. 6 shows the resulting horizontal fields at the four levels designated by asterisks in Table 1.

In the lowest layer an elongated trough is located some 30 km ahead of the squall line, while immediately to the rear and beneath the most intense and mature portion of the line a relative height maximum results. Both of these features are consistent with the generally recognized character of pressure distributions associated with organized convection (see, e.g., Fujita, 1963). In spite of the imposed geostrophic boundary conditions a realistic ageostrophic relationship between observed winds and computed height contours is produced in the interior portion of the grid. Cross-contour components directed from high to low pressure imply that over the southeast part of the grid

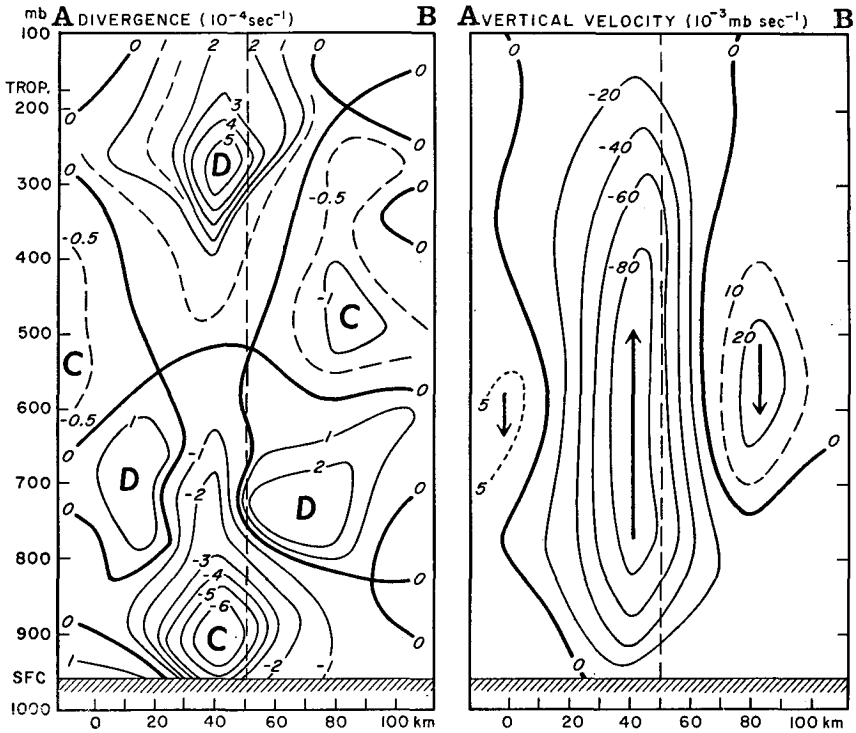

FIG. 5. Cross sections of divergence and vertical velocity along line AB in Fig. 4. Vertical dashed line shows location of grid point where data in Table 1 applies. [10^{-3} mb sec^{-1} $\approx$ 1.5 cm sec^{-1} at 500 mb.]

the southerly flow in this subcloud layer is undergoing acceleration.

The largest gradients across the squall line are computed in the layer centered at 575 mb. Reference to Table 1 shows that the twisting term has the dominant influence on results at this level where horizontal gradients in vertical motion are largest. While ageostrophic components are again found near the active convection, winds well away from the squall line are essentially in geostrophic balance.

In the layer centered on 375 mb, height perturbations are comparatively minor. From the data in Table 1, we see that individual terms are all small and of comparable magnitude in this layer.

Height variations in the divergent layers aloft are exemplified by conditions at 275 mb. The integration yields a distinct ridge of high pressure overlying the squall line which may be explainable through vertical heat transport mechanisms. Presumably the region of high pressure downwind from the large long-lived cell

TABLE 1. Vertical distribution of individual terms (all units 10^{-8} sec^{-2}) in the horizontal divergence equation at the grid point designated in Figs. 5 and 6. Values of magnitude ≥ 10 units are italicized. Asterisks identify layers selected for illustrating integration results in Fig. 6

Layer k	P (mb)	$\partial D/\partial t$	$\left(\mathbf{V}\cdot\nabla D+\omega\frac{\partial D}{\partial p}\right)$	D^2	$\nabla\omega\cdot\partial\mathbf{V}/\partial p$	$-2J(u,v)$	$-f\zeta$	$\nabla^2\phi$
17	175	5.8	− 6.1	6.7	0.9	−0.2	−2.7	− 4.4
16	225	8.2	*−22.6*	*10.7*	0.7	5.2	−1.8	− 0.4
15	275	*13.5*	− 6.8	*35.7*	0.6	−1.3	−0.3	−41.5*
14	325	2.8	*31.6*	2.1	− 5.7	−2.4	−1.5	−27.0
13	375	− 0.3	3.9	0.4	− 2.2	−0.1	−1.2	− 0.5*
12	425	0.0	− 8.3	0.1	*11.1*	1.0	0.1	− 4.0
11	475	− 0.9	− 5.8	0.1	7.3	0.3	0.7	− 1.8
10	525	− 0.6	− 4.2	0.1	*−25.4*	0.8	0.3	28.9
9	575	− 0.6	− 0.8	0.0	*−40.8*	−0.5	1.0	41.6*
8	625	1.5	2.2	0.1	*−18.7*	0.4	−1.3	15.8
7	675	2.9	*−15.9*	0.1	*−10.4*	0.9	−1.3	23.7
6	725	− 6.4	4.5	2.8	− 1.8	−0.7	−1.9	3.6
5	775	− 1.2	*37.7*	1.7	2.5	1.2	−1.4	−40.5
4	825	− 7.2	*37.0*	9.9	− 3.9	1.3	−0.8	−36.3
3	875	*−12.6*	7.0	*43.3*	− 2.0	0.4	−0.3	−35.7*
2	925	*−11.0*	*−12.1*	*33.8*	0.3	1.8	−1.5	−11.3

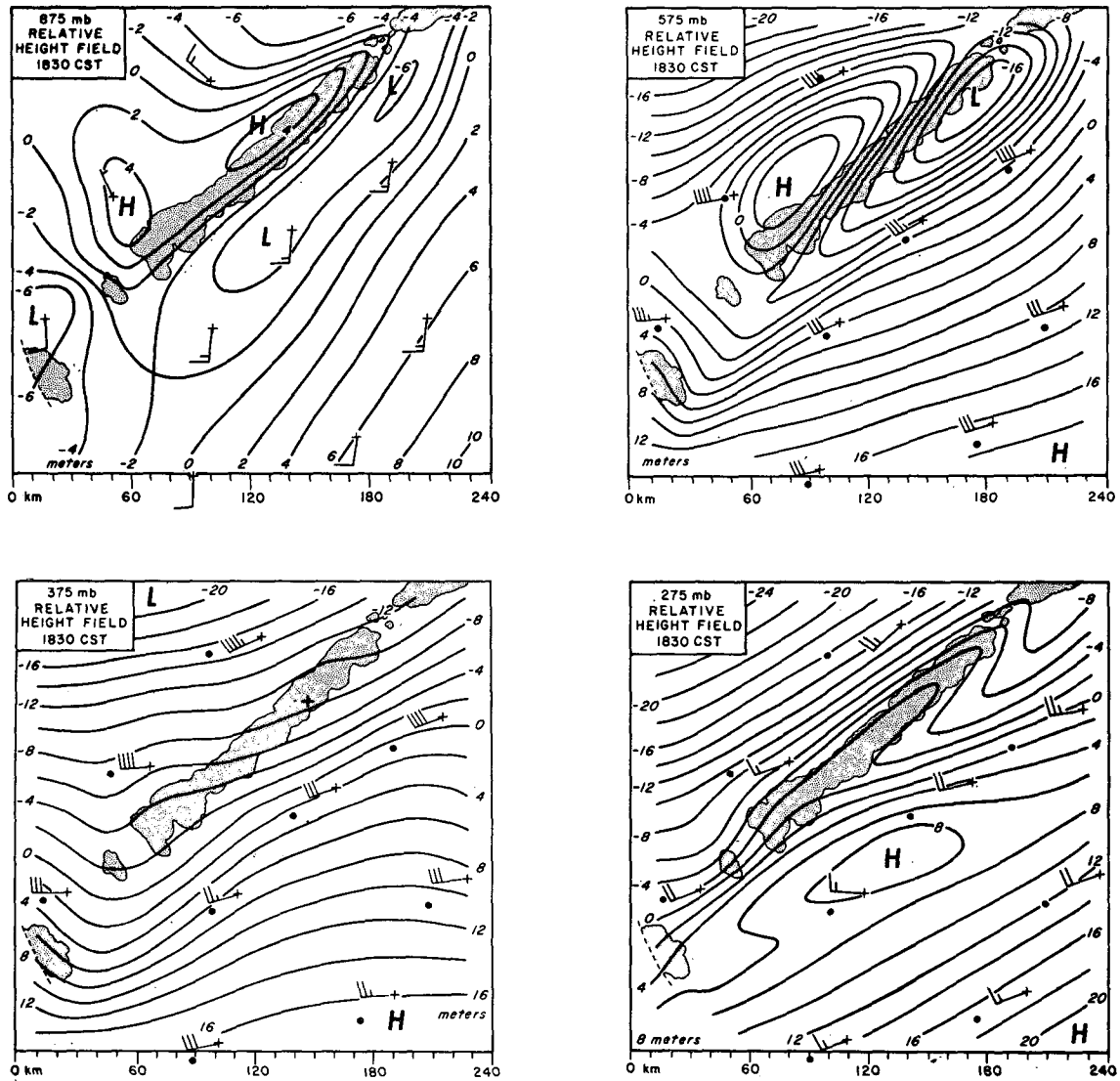

FIG. 6. Relative height fields for layers identified by asterisks in Table 1. Contours at 2 m intervals represent departures from the mean of all grid point values obtained by integrating $\nabla^2\phi = -F(x,y)$, according to conditions discussed in Section 5. Asterisk at the 375-mb level identifies grid point where data in Table 1 apply. Definition of winds is the same as in Fig. 4. Stippled areas show location of radar echoes.

off the southwest corner of the grid is attributable to the same processes.

Results presented in Fig. 6 were tested at all levels by comparing the horizontally differentiated fields of ϕ to assessment of geopotential gradient obtained directly from (9) and (10). Since point comparisons generally agreed to the second digit, the choice of geostrophic boundary conditions was considered justified.

Fig. 7 compares pressure and height perturbations from independent sources. The upper curve is the computed height variation in the 50-mb layer centered on 875 mb taken normal to the squall line axis. Surface pressure recorded at a surface mesonet station affected by squall line passage is reproduced as the bottom curve. Qualitative agreement appears to support the analytical approach.

For a quantitative assessment of the analytical approach we may compare the diagnosed height fields to observed heights at individual rawinsonde stations. To do so we average height values observed at the ten available stations at the 575-mb level and at the time corresponding to the fields shown in Fig. 6. This mean is ascribed to the zero isopleth at 575 mb and a measure of the calculated absolute height is thereby obtained for every point in the grid. Height discrepancies resulting from a point-to-point comparison of observed and calculated heights lead to a standard deviation of ± 10.5 m with departures ranging from -12 to $+18$ m.

These discrepancies are close to those anticipated from system bias and random error sources. Fig. 6 shows that the total gradient across the grid is no

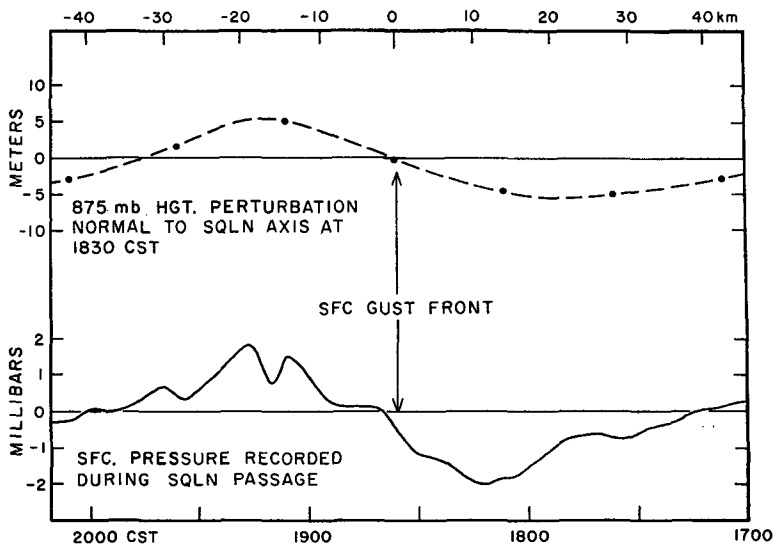

FIG. 7. Computed height perturbation normal to squall line axis compared to observed surface pressure fluctuation recorded during squall line passage. Time-space equivalence is based on squall line motion.

more than 20 m at the lowest level. Since the achievable accuracy in observed height has been demonstrated to be no better than ± 10 m, it is clear that an indirect approach is required for evaluating the height field at the mesoscale.

7. Conclusion

The objective of this study was to derive the horizontal height perturbations associated with mesoscale winds measured in the presence of a well-organized squall line. Results appear to be in qualitative agreement with recognized thunderstorm airflow and pressure distributions. The kinematic features resolved in this and an earlier study (Fankhauser, 1969) indicate that circulations represent the combined effects of synoptic- and convective-scale motions. With estimates of all terms in the equations of motion now available, it should be possible to investigate such important dynamical problems as the mechanisms of energy conversion and momentum transfer between the synoptic and convective scales.

Acknowledgments. The data base for this study was collected under the auspices of the National Severe Storms Laboratory while the author was a member of that group. I thank Brian Hoskins for suggesting the method of adjusting horizontal wind components. Roland Madden and Mel Shapiro made numerous helpful suggestions during the course of the research, and a critical review by Edwin Danielsen significantly influenced the final form of the paper. Sandra Fuller performed all of the numerical calculations and Ralph Coleman drafted most of the figures.

REFERENCES

Barnes, S. L., J. H. Henderson and R. J. Ketchum, 1971: Rawinsonde observation and processing techniques at the National Severe Storms Laboratory. NOAA Tech. Memo., ERL NSSL-53, 246 pp.

Beebe, R. G., and F. C. Bates, 1955: A mechanism for assisting in the release of convective instability. *Mon. Wea. Rev.*, **83**, 1–10.

Cline, A. K., 1973: Curve fitting using splines under tension. *Atmos. Tech.*, No. 3, NCAR, 60–65.

Endlich, R. M., and R. L. Mancuso, 1968: Objective analysis of environmental conditions associated with severe thunderstorms and tornadoes. *Mon. Wea. Rev.*, **96**, 342–350.

Fankhauser, J. C., 1969: Convective processes resolved by a mesoscale rawinsonde network. *J. Appl. Meteor.*, **8**, 778–798.

Fujita, T., 1963: Analytical mesometeorology: A review. *Meteor. Monogr.*, **5**, No. 7, 77–125.

Galway, J. G., 1966: The Topeka tornado of 8 June 1966. *Weatherwise*, **19**, 144–149; 160.

House, D. C., 1958: Air mass modification and upper-level divergence. *Bull. Amer. Meteor. Soc.*, **39**, 137–143.

——, 1961: The divergence equation as related to severe thunderstorm forecasting. *Bull. Amer. Meteor. Soc.*, **42**, 804–816.

Jenne, R. L., D. H. Joseph, E. C. Ridley and R. C. Fabec, 1972: The Bendix Datagrid graphic digitizing system: Operational procedure and available software. NCAR Tech. Note, NCAR-TN-IA-78, 164 pp.

Kreitzberg, C. W., and W. E. Brockman, 1966: Computer processing of mesoscale rawinsonde data from Project Stormy Spring. AFCRL-66-97, Spec. Rept. No. 41, 35 pp.

Lenhard, R. W., 1973: A revised assessment of radiosonde accuracy. *Bull. Amer. Meteor. Soc.*, **54**, 691–693.

Madden, R. A., E. J. Zipser, E. F. Danielsen, D. H. Joseph and R. Gall, 1971: Rawinsonde data obtained during the Line Islands Experiment, Volume I: Data reduction procedures and thermodynamic data. NCAR Tech. Note, NCAR-TN/STR-55, 71 pp.

O'Brien, J. J., 1970: Alternative solutions to the classical vertical velocity problem. *J. Appl. Meteor.*, **9**, 197–203.

Smith, P. J., 1971: An analysis of kinematic vertical motions. *Mon. Wea. Rev.*, **99**, 715–724.